

Article

Numerical Study on Dynamic Characteristics of Vehicle Entering Water at High Speed

Zhenpeng Liu ^{1,2}, Yao Shi ^{1,2,*} , Guang Pan ^{1,2} and Hairui Zhao ^{1,2}

¹ School of Marine Science and Technology, Northwestern Polytechnical University, Xi'an 710072, China

² Key Laboratory of Unmanned Underwater Vehicle Technology of Ministry of Industry and Information Technology, Northwestern Polytechnical University, Xi'an 710070, China

* Correspondence: shiyao@nwpu.edu.cn

Abstract: Aiming at a design for buffering and load reduction configuration for a large-scale (diameter greater than 500 mm) vehicle entering water at high speed (greater than 100 m/s), a numerical model for a vehicle entering water at high speed was employed based on an arbitrary Lagrange-Euler (ALE) algorithm. Combined with modal analysis and shock response spectrum, the influence of the head cap on the dynamic characteristics of the structure was analyzed. The results showed that the peak value and pulse width of the impact load on the vehicle increased with the increase in the speed of water entry. The existence of the head cap increased the complexity of the forces on the vehicle during the process of water entry. The initial formation of the cavity was greatly affected by the head cap. The head cap and the vehicle separated in the later stage of the water entry. During the process of water entry, the shell of the vehicle was mainly compressed and bent and the head cap reduced the deformation. The relevant conclusions of this paper can provide some input for the design of a new buffering structure and vehicle shell.

Keywords: high-speed water entry; numerical calculation; modal analysis; shock response spectrum



Citation: Liu, Z.; Shi, Y.; Pan, G.; Zhao, H. Numerical Study on Dynamic Characteristics of Vehicle Entering Water at High Speed. *J. Mar. Sci. Eng.* **2022**, *10*, 1387. <https://doi.org/10.3390/jmse10101387>

Academic Editors: K. Reza Kashyzadeh and Mahmoud Chizari

Received: 19 August 2022
Accepted: 23 September 2022
Published: 28 September 2022

Publisher's Note: MDPI stays neutral with regard to jurisdictional claims in published maps and institutional affiliations.



Copyright: © 2022 by the authors. Licensee MDPI, Basel, Switzerland. This article is an open access article distributed under the terms and conditions of the Creative Commons Attribution (CC BY) license (<https://creativecommons.org/licenses/by/4.0/>).

1. Introduction

The cross-medium vehicle combines the dual advantages of high speed and long range, and is a key direction for the development of new types of vehicle. In the process of transferring from air ballistics to water ballistics, the vehicle will experience a process of high-speed water entry. In this process, due to the sudden change of medium density, complex turbulent flow, large deformation of free surface and strong coupling between multiple phases and many other physical effects, the vehicle will be subjected to a huge impact load, which may lead to problems such as ballistic instability and structural damage of the vehicle. It is of great engineering significance to study dynamic characteristics such as the structural response of the vehicle in this process for the design of the shell and external buffer measures of the vehicle.

Research devoted to the impact load of structures entering water is carried out in three directions [1], namely, theoretical analysis, numerical calculation and experimental studies. The development of water entry theory started with von Karman. When studying the forced landing of a seaplane, the compressibility of fluid and the influence of flow field movement on the object were ignored. The water entry impact theory of wedge was established by using the momentum conservation theorem, and the water entry impact pressure of wedge was obtained. Miloh [2] carried out an analytical study on the case of a rigid sphere obliquely entering an ideal incompressible fluid. Under the assumption that the free surface is an equal potential energy plane, the asymptotic expression of the added mass and the hydrodynamic force was obtained. Reinhard [3] analyzed the problem of two-dimensional elastic plate collision with calm water surface, and studied the influence of the flexibility of the plate and the elastic vibration of the plate on the

hydrodynamic load and fluid flow. Hulin et al. [4] analyzed the influence of gravity in the process of two-dimensional axisymmetric objects entering water, and proposed a water impact model considering the influence of gravity, which is an extension of the Wagner model. It is difficult to establish a mathematical model by theoretical analysis, which often needs to introduce many assumptions. Moreover, most of the existing theoretical research objects are simple geometry, and the relevant theories cannot be directly applied to engineering practice.

With the development of computer technology, numerical research has the advantages of high repeatability and low cost. It is the first choice for many scholars to study the phenomenon of water impact. Different from Computational Fluid Dynamics (CFD), the focus of impact load research is the structural response of structure and fluid under bidirectional dynamic load, rather than the movement of fluid. A common method is to use the Lagrange grid to describe the small deformation of the structure in the process of water entry, and use the Euler grid to capture the large deformation of the free surface. Ryzhakov et al. [5] applied the Particle Finite Element Method (PFEM) to simulating the sea landing of an unmanned aerial vehicle. They modeled the impact of the vehicle against the water surface and analysed the main kinematic and dynamic quantities. Sun et al. [6] employed a finite element model of high-speed water entry of a large-scale projectile based on a multi-material arbitrary Lagrange–Euler (multi-material ALE) algorithm, analyzed the impact of the change of nose shape on the overall load of the projectile, and the influence of the change of water entry angle on the overall load and ballistic stability of the projectile. Wang et al. [7] carried out dynamic analysis of aircraft forced landing on water based on a structured arbitrary Lagrange–Euler (S-ALE) algorithm, extracted the change law of aircraft pitch attitude and overload, and compared it with relevant results of the experiment. He et al. [8] studied the slamming of three typical sections (bow, parallel midship and stern) of a container ship under three different load conditions (no-load weight, half load weight and full load weight of the ship) using an ALE algorithm, and analyzed and discussed the influence of ship load and section shape on water entry impact, which is helpful to analyze the influence of load on ship slamming at the early stage of ship design. Li et al. [9] used an arbitrary Lagrange–Euler (ALE) algorithm to conduct numerical simulation on the high-speed water entry of a vehicle (diameter is 240 mm) with head cap, and analyzed the failure mode of the nose cap and the load reduction performance of the head cap. Wei et al. [10] carried out numerical calculation and analysis on the high-speed water entry of a vehicle (diameter is 324 mm) with buffer components based on ALE method, obtained the dynamic damage process of the nose cap and the foam, studied the motion parameters of the vehicle during the water entry process, and analyzed the performance of different buffer schemes. Sun et al. [11] studied the load reduction characteristics of the buffering device by using the coupled Euler–Lagrange (CEL) method, and obtained the law that the load reduction performance of a certain water entry velocity varies with the relative density of aluminum foam. Quan et al. [12] used a coupled Euler–Lagrange solver to study the load reduction performance of the head cap, and analyzed the impact resistance, damage mode of the head cap and the process of the cavity development under different velocity and angle of water entry. At the same time, computational fluid dynamics is also a common means for some scholars to study the phenomenon of water entry. Yu et al. [13] conducted a numerical study on the free fall of a sphere by using the transient Reynolds average method, and discussed the influence of impact speed, radius, mass and other parameters of the sphere on the impact force and acceleration of the sphere. Qiu et al. [14] established a mathematical model of the free fall of a lifeboat to the water by using the strip theory and Kane method; the sled force acting on the ship was calculated, and the slamming force of the ship when entering the water was solved. Li et al. [15] used a ZGB cavitation model and SST turbulence model based on the RANS method to numerically study the influence of cavitation head structure of a high-speed projectile on ballistic stability in the process of water entry, and studied the influence of angle of cavitation head and diameter of cavitation body on ballistic stability and flow characteristics. Yang et al. [16] presented a two-phase

Smoothed Particle Hydrodynamics (SPH) model for simulating the water entry of a cavity body, investigating the dynamics phenomena in the coupling process between cavity body and two-phase flow and showing the effects of air, mass and the sizes and incline angles of the cavity body on the dynamic characteristics of cavity body and two-phase flows. Sun et al. [17] studied the characteristics of slamming pressure and impact force of the trimaran profile through computational fluid dynamics, and analyzed the effects of velocity and acceleration on the slamming pressure and impact force. Fan et al. [18] conducted a numerical study on the phenomenon of a vehicle entering the water at free and constant speed, studied the evolution of cavitation under different head shapes, tail shapes and impact speeds, compared the resistance characteristics of the vehicle under free and constant impact speeds, and analyzed the flow characteristics of the flow field. Wang et al. [19] used computational fluid dynamics to simulate the process of a cylinder vertically entering an ice-free water surface and an ice–water mixture at low speed based on the Finite Volume Method (FVM), the Volume of Fluid method (VOF), the continuous surface force (CSF) model and overlapping grid technology, providing a useful reference for the design of a new type of cross-medium projectile in an extremely low temperature environment in winter. Because there is a certain deviation between numerical calculation and physical reality when establishing a mathematical model, and some practical factors are difficult to consider, experimental research is often used as a supplement to numerical calculation to verify the correctness and accuracy of the numerical model.

For research experiments in water entry, people need to pay attention to the evolution process of cavity and flow field in the process of water entry, which is closely related to the force situation of the structure and the change of ballistic attitude. Chen et al. [20] used high-speed photography technology to conduct experimental research on the high-speed oblique entry of projectiles into water, and studied the formation, growth and pinch off of cavitation, as well as the tail beat motion, vortex shedding, splash, ascending jet, trajectory deflection and surface closure, and established a prediction formula for the underwater cavitation profile and maximum cavitation size. Panciroli et al. [21] carried out an experiment of the flexible wedge impacting the static water surface at a vertical speed, studied the influence of the wedge bending stiffness, static lift angle and drop height on the formation of cavitation, and revealed the mechanism of cavitation formation. Zhou et al. [22] used high-speed laser shadow and schlieren flow field display technology to study the deformation and breaking of the air–water interface and gave the evolution image of the flow field of the high-speed oblique penetration of projectiles into the water. Chen et al. [23] conducted an experimental study on the ballistic stability of high-speed projectiles entering the water by using dynamic photography, and quantitatively expressed the influence of head shape, impact speed and water entry attitude angle on the ballistic stability of slender projectiles. Song et al. [24] carried out a high-speed oblique water entry experiment of a cylindrical projectile by using high-speed photography technology, and explored the influence of projectile shape and initial conditions on the development and change of cavitation. She et al. [25] used time-resolved particle image velocimetry (TR-PIV) technology to test the flow field of wedges with different bottom lift angles during water entry, analyzed the motion response and flow field during water entry, and discussed the accuracy and applicability of the pressure reconstruction scheme based on TR-PIV. Liu et al. [26] developed an experiment system, captured the shock waves in the air and water caused by oblique water entry, and observed the fluctuation and instability of the air–water interface of the tail bubble during horizontal water entry. Sun et al. [27] studied the flow field and the characteristics of impact load of an aerated cylinder when it entered the water vertically and obliquely, and studied the influence of ventilation and angle of attack on impact load and characteristics of flow field. Tang et al. [28] studied the air cushion effect when a trimaran enters the water, proposed a test method and a new model design, and analyzed the influence of the model opening size and the initial release height on the slamming pressure.

As far as the existing bibliography is concerned, it is mainly aimed at the ballistic attitude or the development and evolution of cavitation during the high-speed water entry of the vehicle. Few studies aim at understanding the dynamic characteristics such as the structural response of the shell during high-speed water entry. The conclusion of this paper provides an input for the design of a newer load-reduction device for high-speed water entry of a vehicle.

The structure of this article is as follows. The second section introduces the configuration and geometric parameters of the vehicle and the head cap, then introduces the numerical model. In the third section, the time-domain characteristics of cavity and impact load are analyzed. In the fourth section, the dry modal analysis of the vehicle is carried out, and the different modal shapes and corresponding natural frequencies are obtained. Then, the shock response spectrum of the impact load obtained in the third section is calculated. Finally, the structural response of the shell in the process of water entry is solved by combining modal analysis and shock response spectrum. The last section introduces the main conclusions of this paper.

2. Model Building

2.1. Geometric Model

Under the same water entry conditions, the impact load on the vehicle is mainly affected by the shape of its head and the maximum cross-sectional area. The external structures such as propellers and fins and rudders outside the vehicle are ignored, and the vehicle is simplified as a revolving shell. The vehicle is a torpedo named MK-48, the total length is 5850 mm, and the maximum diameter is 533 mm. The head cap is composed of nose cap, buffer, locating structure and connector, as shown in Figure 1 [29]. The nose cap adopts the shape of a pointed arch, and the pointed arch angle is 50° , which can carry the pressure during flight and provide a good aerodynamic shape. At the same time, there is a prefabricated groove on the nose cap [30], so that the nose cap can be broken along the groove after hitting the water. The total length of the buffer is 600 mm, which plays the role of absorbing energy and reduces the impact load of water entry. The locating structure defines the relative position between the head cap and the vehicle. The connector relies on its own deformation to provide friction to closely connect the head cap with the vehicle.

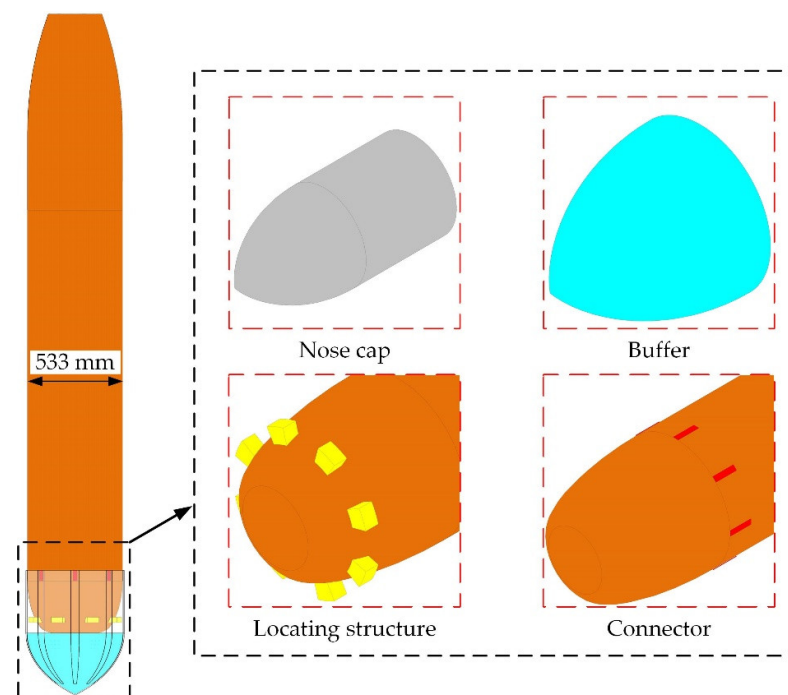


Figure 1. Schematic diagram of the head cap.

2.2. Numerical Model

The ALE algorithm [31] combines the advantages of the Lagrange algorithm and the Eulerian algorithm, solves the problem that Eulerian mesh is not accurate in capturing a small deformation of structure, and overcomes the difficulty that Lagrangian mesh is easily distorted when dealing with large deformation, resulting in oscillation of numerical calculation results. A numerical model based on the ALE algorithm in the commercial software (LS-DYNA) is used to simulate the high-speed water entry of the vehicle.

The control equation of the ALE algorithm is composed of mass conservation equation, momentum conservation equation and energy conservation equation, as shown in Equations (1)–(3):

$$\frac{\partial \rho}{\partial t} = -\rho \frac{\partial v_i}{\partial x_i} - w_i \frac{\partial \rho}{\partial x_i} \tag{1}$$

$$v \frac{\partial v_i}{\partial t} = \sigma_{ij,j} + \rho b_i - \rho w_i \frac{\partial v_i}{\partial x_j} \tag{2}$$

$$\rho \frac{\partial E}{\partial t} = \sigma_{ij} v_{i,j} + \rho b_i v_i - \rho w_j \frac{\partial E}{\partial x_j} \tag{3}$$

where ρ is the density of the fluid; x is the coordinate in the Euler coordinate system; v is the velocity of the material, and the subscript of $v_{i,j}$ represents the differential of the pair; u is the velocity of the mesh; w is the relative velocity given by $w = v - u$; E is internal energy; σ_{ij} is the stress tensor, and the subscript of $\sigma_{ij,j}$ represents the differentiation of j ; b is the volume force load on the fluid.

The material constitutive model of the vehicle, locating structure, connector and nose cap is a bi-linear elastic–plastic model (as shown in Figure 2), and its stress–strain curve can be expressed by Equation (4). The parameters of material are shown in Tables 1–3. The constitutive model of buffer is defined by the input stress–strain curve (as shown in Figure 3) and the parameters of material are shown in Table 4. The motion of water is described by Equations (4) and (5). The parameters of water are shown in Table 5 and the parameters of equation of state are shown in Table 6. The motion of air is described by Equation (6). The parameters of air are shown in Table 7 and the parameters of equation of state are shown in Table 8 [29].

$$\sigma = \begin{cases} E\varepsilon, 0 \leq \varepsilon \leq \sigma_s/E \\ E_t\varepsilon + \sigma_s(1 - E_t/E), \sigma_s/E < \varepsilon \end{cases} \tag{4}$$

where σ is the nominal stress, E is the Young’s modulus, ε is the nominal strain, σ_s is the yield stress, E_t is the tangent modulus.

$$p = \frac{\rho C^2 \mu [1 + (1 - \frac{\gamma_0}{2})\mu - \frac{\alpha}{2}\mu^2]}{[1 - (S_1 - 1)\mu - S_2 \frac{\mu^2}{\mu+1} - S_3 \frac{\mu^3}{(\mu+1)^3}]^2} + (\gamma_0 + \alpha\mu)E \tag{5}$$

$$\mu = \frac{1}{V} - 1 \tag{6}$$

$$p = C_0 + C_1\mu + C_2\mu^2 + C_3\mu^3 + (C_4 + C_5\mu + C_6\mu^2)E \tag{7}$$

where p is the pressure, ρ is the density, C is the velocity of sound, γ_0 is the Gruneisen constant, α is the first-order correction of volume, S_1, S_2, S_3 are the dimensionless coefficients, V is the relative volume, and E is the internal energy per unit volume in the initial state.

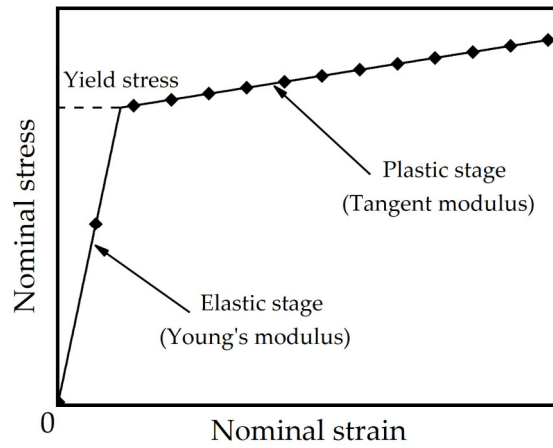


Figure 2. Schematic diagram of bi-linear elastic–plastic model.

Table 1. Material parameters of vehicle and locating structure.

Density/(kg·m ⁻³)	Young's Modulus/GPa	Poisson's Ratio	Yield Stress/MPa	Tangent Modulus/GPa
2700	75	0.33	275	1.33

Table 2. Material parameters of connector.

Density/(kg·m ⁻³)	Young's Modulus/GPa	Poisson's Ratio	Yield Stress/GPa	Tangent Modulus/GPa
7830	207	0.3	4	50

Table 3. Material parameters of nose cap.

Density/(kg·m ⁻³)	Young's Modulus/GPa	Poisson's Ratio	Yield Stress/MPa	Failure Strain
1160	3.5	0.34	1.01	0.1

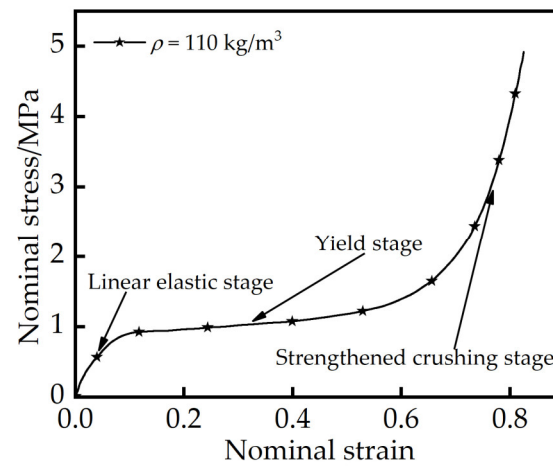


Figure 3. Compression stress–strain curve of buffer.

Table 4. Material parameters of buffer.

Density/(kg·m ⁻³)	Young's Modulus/MPa	Poisson's Ratio	Tensile Stress Cutoff/MPa
90	129	0.02	1.6

Table 5. Material parameters of water.

Density/(kg·m ⁻³)	Pressure Cutoff/Pa	Viscosity Coefficient
998.21	−10.0	0.0008684

Table 6. State equation parameters of water.

C/(m·s ⁻¹)	S ₁	S ₂	S ₃	γ ₀	A	E/J	V ₀
1480	2.56	−1.986	0.23	0.5	0.47	0	1

Table 7. Material parameters of air.

Density/(kg·m ⁻³)	Pressure Cutoff/Pa	Viscosity Coefficient
1.25	−1.0	0.000017465

Table 8. State equation parameters of air.

C ₀ , C ₁ , C ₂ , C ₃ , C ₆	C ₄ , C ₅	E/kJ	V ₀
0	0.4	250	1

2.3. Model Validation

The employed numerical model is tested and verified. The experiment device and numerical model are shown in Figure 4. High-pressure air is used as the power for the launch of the model, and a high-speed camera is installed in the tank to capture the evolution process of the water entry trajectory and the cavity. The model has a maximum outer diameter of 200 mm, a total length of 483 mm, a mass of 15 kg and is composed of a head section and a rear end cover.

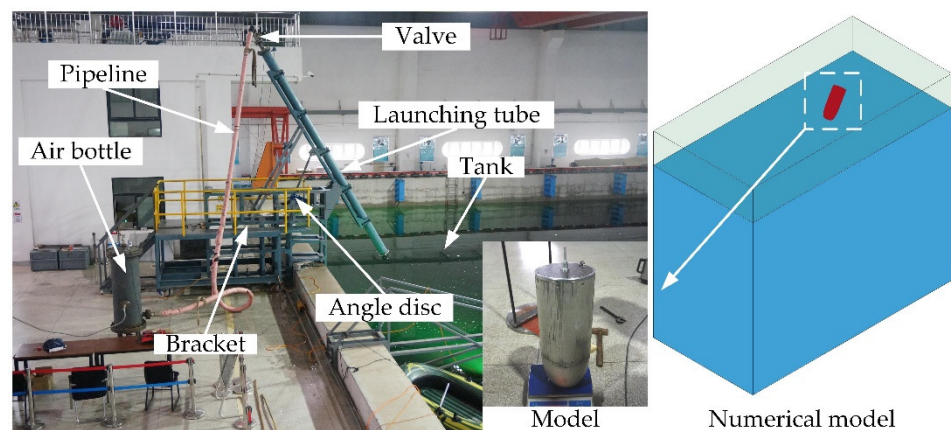


Figure 4. Schematic diagram of experimental device and numerical model.

During the experiment, the pressure of compressed air is calculated and adjusted according to the empirical formula to make the launching speed of the model 100 m/s, and the angle disk of the launching device is adjusted to make the launching angle 60°. Since the launching nozzle is close to the water surface, it can be considered that the speed of the model is 100 m/s and the angle is 60°.

Figure 5 shows a comparison between the cavity obtained by simulation at different times and the images taken by the underwater high-speed camera, which records the process of cavity expansion in the early stage of the model entering the water. It can be seen that the macroscopic change trend of the two is consistent and the coincidence is high.

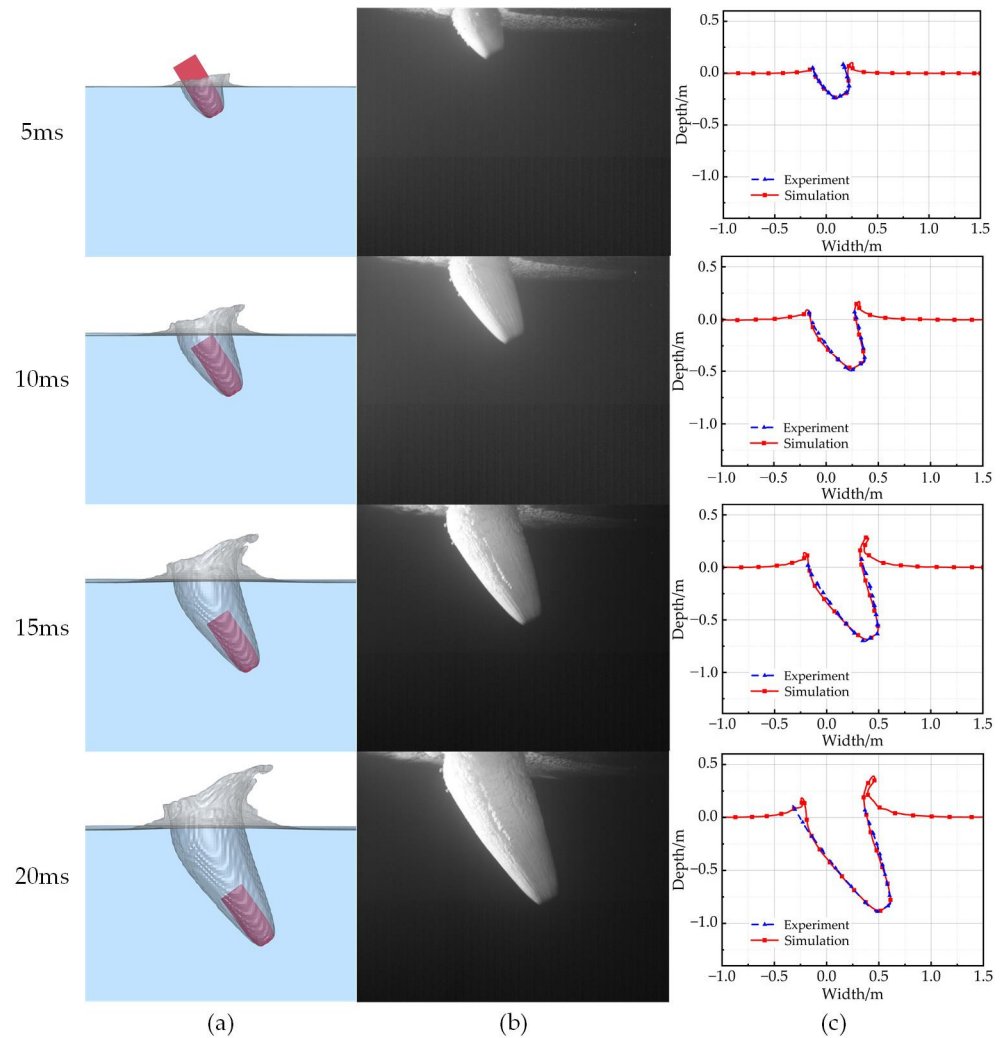


Figure 5. Cavitation comparison between simulation and experiment: (a) simulation, (b) experiment, (c) comparison.

Figure 6 shows the comparison of axial acceleration between experiment and simulation, and Figure 7 shows the comparison of radial acceleration between experiment and simulation. It can be seen from the figure that the acceleration obtained from the experiment and the simulation basically have the same trend with time. Because high-pressure gas is used to launch the model and the built-in triaxial acceleration sensor is used to measure and record the information of acceleration, there are some factors that are difficult to consider for simulation, such as the interference of residual gas in model attitude after the model is launched from the launch tube and the vibration of the sensor itself during the experiment. Therefore, there are many fluctuations in the curve of acceleration measured in the experiment. The absolute value of the relative error of the peak of axial acceleration is 2.97%, and the absolute value of the peak of radial acceleration is 10.62%. The numerical model adopted in this paper meets the actual engineering needs of calculation of impact load of high-speed water entry.

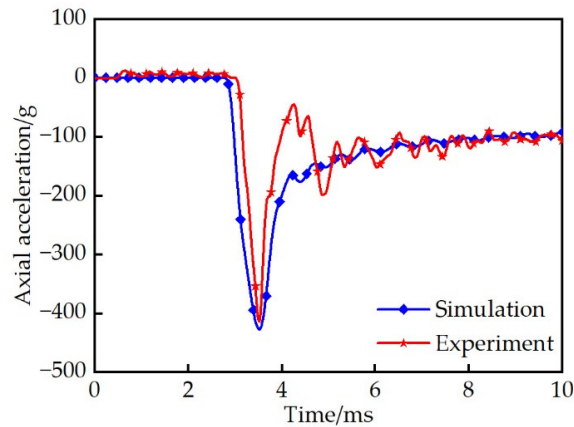


Figure 6. Comparison of axial acceleration between experiment and simulation.

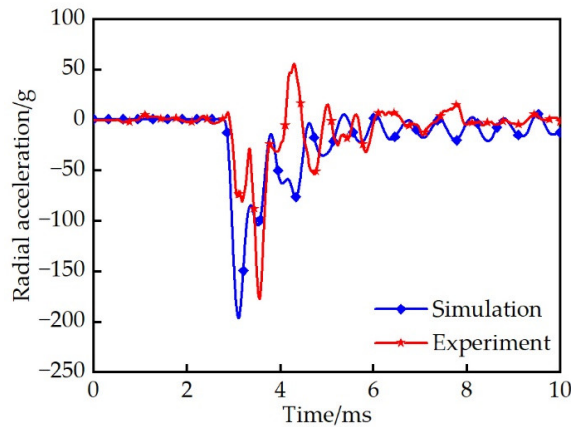


Figure 7. Comparison of radial acceleration between experiment and simulation.

The mesh size of the vehicle and the head cap is 10 mm, and the mesh size of the water and air is changed to 10 mm, 20 mm, 30 mm, 40 mm and 50 mm, respectively, to verify grid independence.

Figure 8 shows the time–history of the impact acceleration coefficient under different mesh sizes, and Figure 9 shows the peak value and pulse width of the impact acceleration coefficient under different mesh sizes. It can be seen from the figure that when the mesh sizes are different, the change trend of the time–history of the acceleration coefficient is basically the same, and with the reduction of mesh size, the peak value and peak pulse width of the acceleration coefficient tend to be consistent.

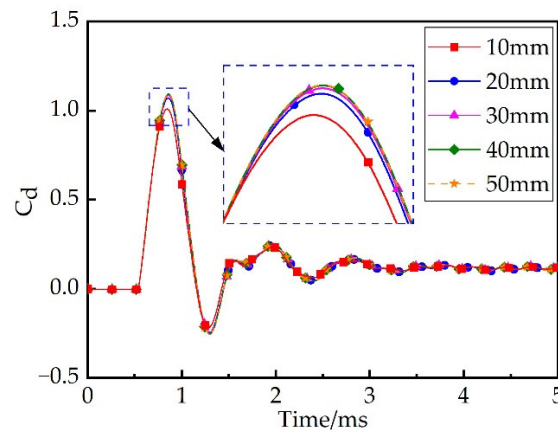


Figure 8. Acceleration coefficient of mesh with different size.

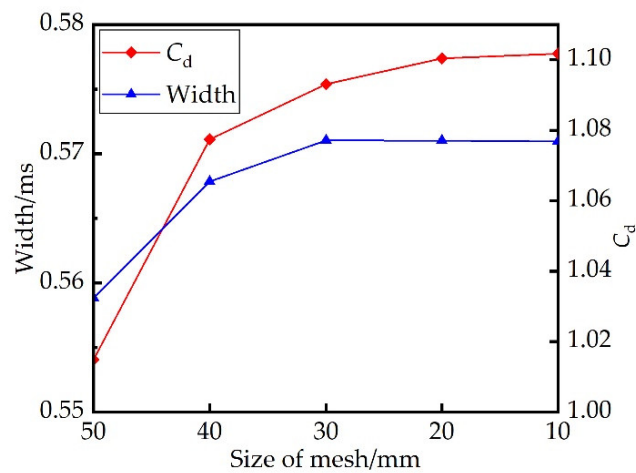


Figure 9. Peak and peak pulse width of mesh with different size.

Considering the accuracy and efficiency of calculation, the mesh size of the vehicle and head cap is 10 mm, the mesh size of water and air is 40 mm, and the total number of divided mesh is 8,627,528.

The interference of wall effect on the calculation results should be minimized during the numerical calculation. Therefore, the dimensions of calculation domain is 10 m × 6.4 m × 12 m, the bottom is set as fixed boundary condition, and the surrounding wall is set as non-reflective boundary condition to reduce the influence of the wall effect on the results, as shown in Figure 10. The calculation situations are shown in Table 9.

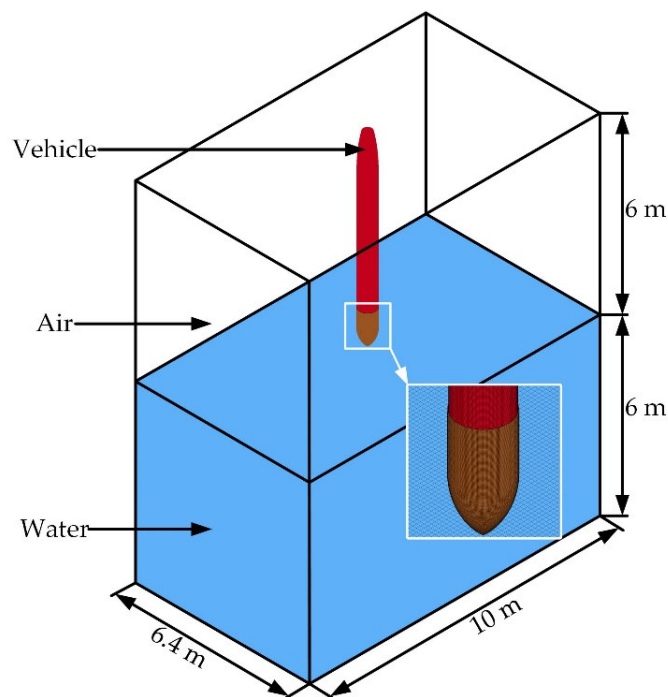


Figure 10. Schematic diagram of the calculation domain.

Table 9. Situations of simulation.

Number	Velocity/(m·s ⁻¹)	Angle/°	Head Cap
1	100	90	Y
2	150	90	Y
3	200	90	Y
4	250	90	Y
5	300	90	Y
6	100	90	N
7	150	90	N
8	200	90	N
9	250	90	N
10	300	90	N

Y represents that the vehicle enters the water with head cap; N represents that the vehicle enters the water without head cap.

3. Characteristic Analysis of Time Domain

3.1. Water Entry of Vehicle without Head Cap

Figure 11 shows a schematic diagram of cavity when the vehicle vertically enters the water at a speed of 100 m/s, and Figure 12 shows the velocity vector of flow field. In order to keep the height of the end face of the head from the water surface consistent at the initial time when the vehicle is without the head cap and with the head cap, the distance between the end face of the head and the water surface when the vehicle enters the water without head cap is set as the length of the head cap.

When the vehicle enters the water vertically, a moving flow field will be established in the static free surface. It can be seen from the figure that the front end of the head of the vehicle is first wetted, giving a certain kinetic energy to the water in a very short time, resulting in a large lateral velocity of fluid, which causes the water to be displaced to both sides. The air moving with the vehicle forms a cavity around the head. At the same time as cavitation occurs, as the water is squeezed with an upward velocity, splashing also occurs, and a bulge higher than the initial free surface appears around the vehicle. When the water obtains enough kinetic energy and the velocity is high enough, a crescent shaped splashing film appears at the connection between the edge of the cavity and the free surface.

With the continuous increase in the depth of the vehicle, the air continuously flows into the cavity to accelerate the expansion. However, at this time, the wall surface of the cavity near the free surface presents a contraction trend. On the one hand, the increase in depth leads to an increase in hydrostatic pressure. When the pressure in the cavity is lower than the pressure of the surrounding water, the wall of the cavity will show a contraction movement. On the other hand, due to the high speed of the vehicle entering the water, the whole cavity is continuously elongated, resulting in the air being too late to enter the cavity, which is also an important factor that causes the internal pressure of the cavity to decrease.

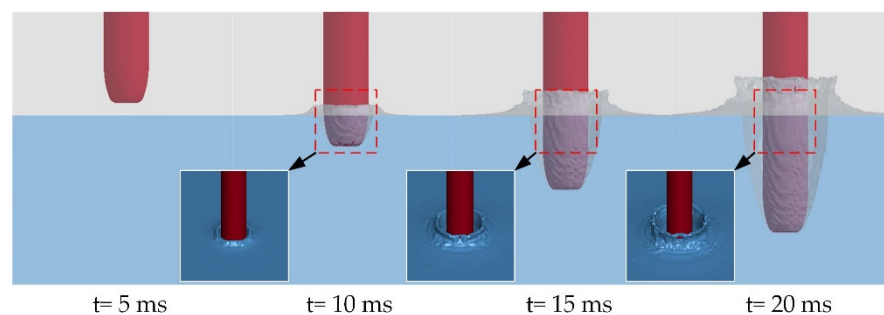


Figure 11. Cavity of vehicle entering water at speed of 100 m/s without head cap.

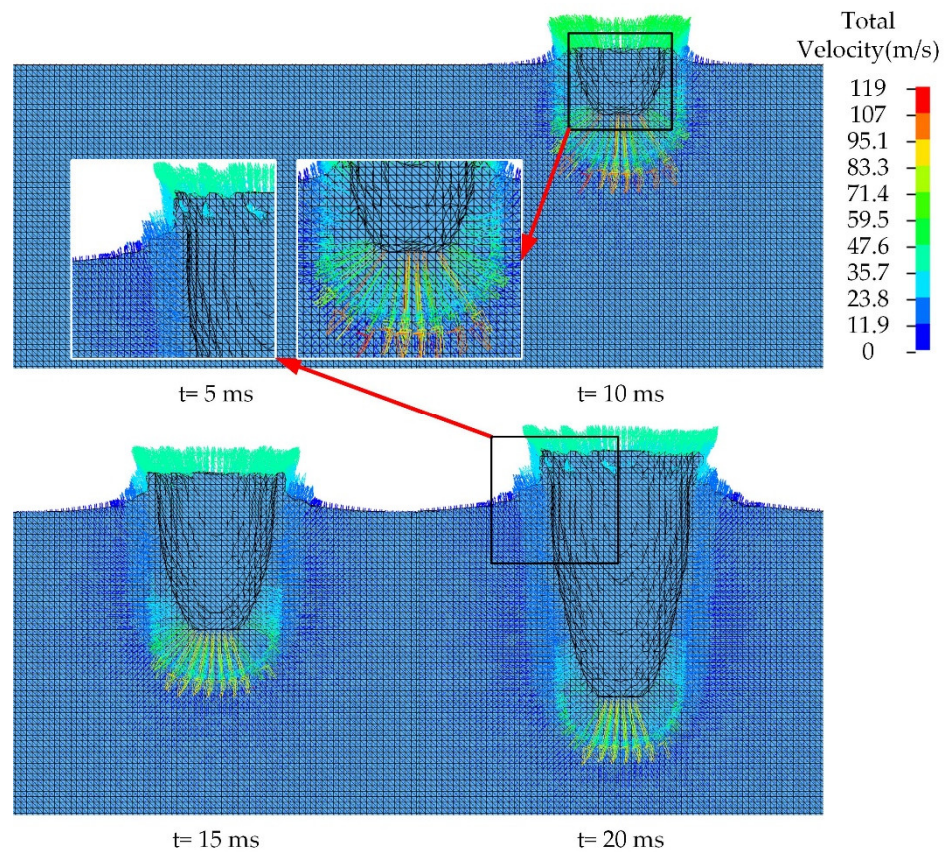


Figure 12. Schematic diagram of velocity of flow field.

Figure 13 shows the time–history of the acceleration of the vehicle when it enters the water vertically at a speed of 100 m/s under different mesh sizes. Observing the red curve in the figure, it is found that without the head cap, the head of the vehicle will be subjected to a huge impact load when it touches the water. The impact load will rise rapidly to the peak value and fall within nanoseconds. At the peak value, the vehicle is likely to be damaged.

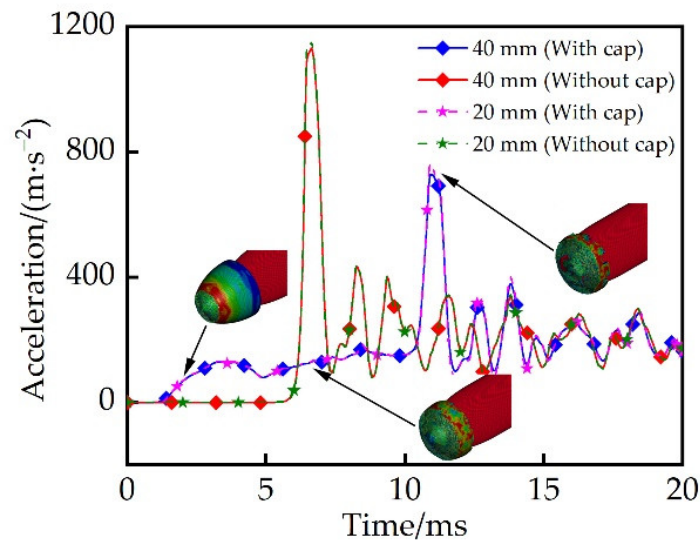


Figure 13. Acceleration of vehicle vertical water entry at 100 m/s.

Figure 14 shows the time–history of impact acceleration when the vehicle enters the water vertically at different speeds. It can be seen from the comparison that the change law of impact load at different speeds is basically the same, the peak of load appears when the head of the vehicle hits the water surface at the early stage of water entry, and the duration of peak is short. With the deepening of the water entry process, the head of the vehicle constantly slams with the fluid, and the impact load also shows a small range of fluctuations. With the increase in the speed of water entry, the peak value and pulse width of the impact load will also increase.

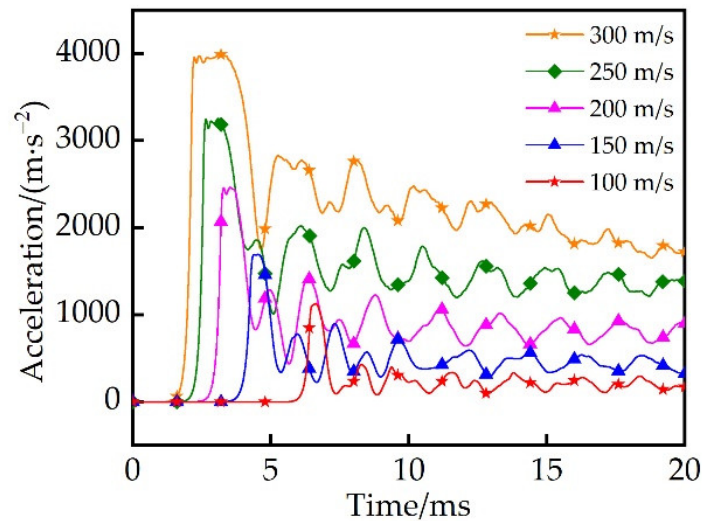


Figure 14. Time–history acceleration at different speed of water entry.

3.2. Water Entry of Vehicle with Head Cap

When the vehicle enters the water vertically with the head cap, the evolution of the cavity and the vector of velocity of the flow field are shown in Figures 15 and 16. It can be seen from the figures that the nose cap first collides with the free surface, generating compression waves in the nose cap and the water, respectively. The compression waves in the water cause the fluid to generate wave motion patterns to transmit and dissipate the energy. The compression waves in the nose cap cause local damage and failure at the front end of the nose cap and form an approximately circular hole to expose the buffer material inside, then the buffer material is compressed by the water and the vehicle, and the impact load is transmitted to the vehicle.

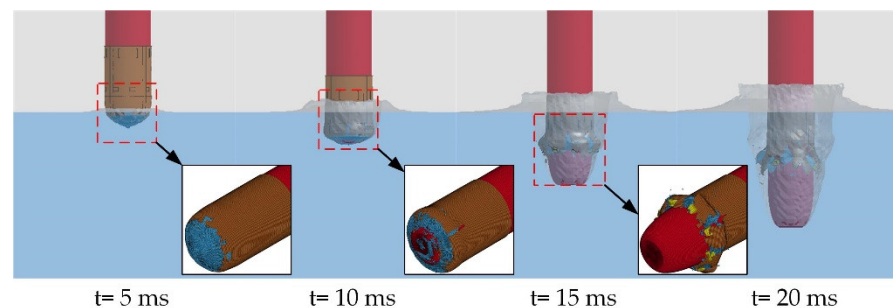


Figure 15. Cavity of vehicle entering water at speed of 100 m/s with head cap.

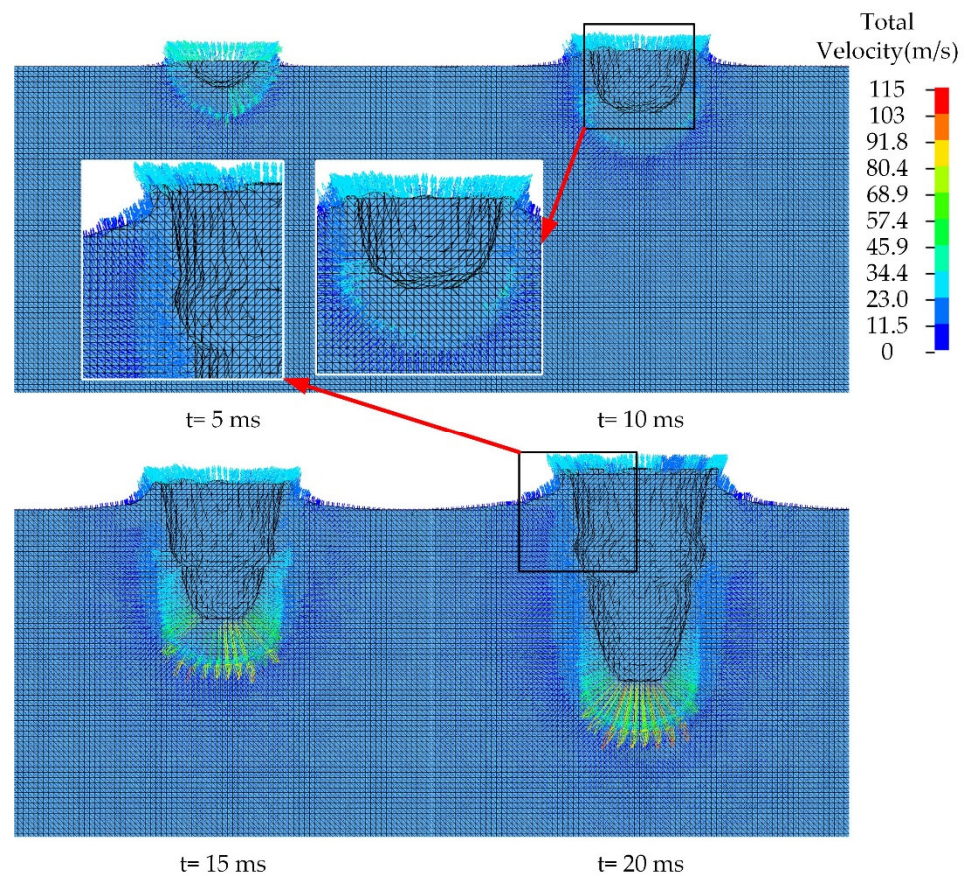


Figure 16. Schematic diagram of velocity of flow field.

With the increase in depth, the hole presented by the nose cap failure also increases, and the edge of the hole also curls inward, warping and deforming, exposing more buffer material. In the early stage of water entry, when the vehicle enters the water with head cap, the size of the cavity is larger and the wall surface is coarser. However, in the later stage of water entry, the cavities of the two are basically the same, which indicates that the development and formation of the cavity in the early stage of water entry is greatly affected by factors such as the shape of the head.

It can be seen from the time–history of impact load (blue curve in Figure 13) of the vehicle entering the water vertically at the speed of 100 m/s that when the buffer material is compressed, its deformation goes through three stages: linear elastic stage, yield stage and strengthened crushing stage.

The first deformation stage is the linear elastic stage. At this time, the impact load rises relatively slowly, and the impact load is softer. The buffer improves the impact environment of the vehicle at the early stage of water entry. When the internal stress of the buffer material reaches its yield stress, its deformation enters the yield stage. When the buffer material is in the yield stage, it can maintain a nearly constant stress under a large strain state and absorb energy. Correspondingly, the impact load in the figure is kept within a certain level range, neither rising nor falling significantly. With the continuous downward movement of the vehicle, the buffer material enters the stage of strengthening and breaking. When the buffer material is punctured by the vehicle, the impact load peaks. Then the head directly contacts the water, and the two continue to slam. The impact load fluctuates within a certain level. Comparing the time–history of impact load under different speeds of water entry (Figure 17), it can be seen that with the increase in speed, and the shorter the failure time of the head cap, the impact acceleration of the vehicle is still a large value. When the water entry speed is high, the traditional head cap has a limited effect on buffering and load reduction.

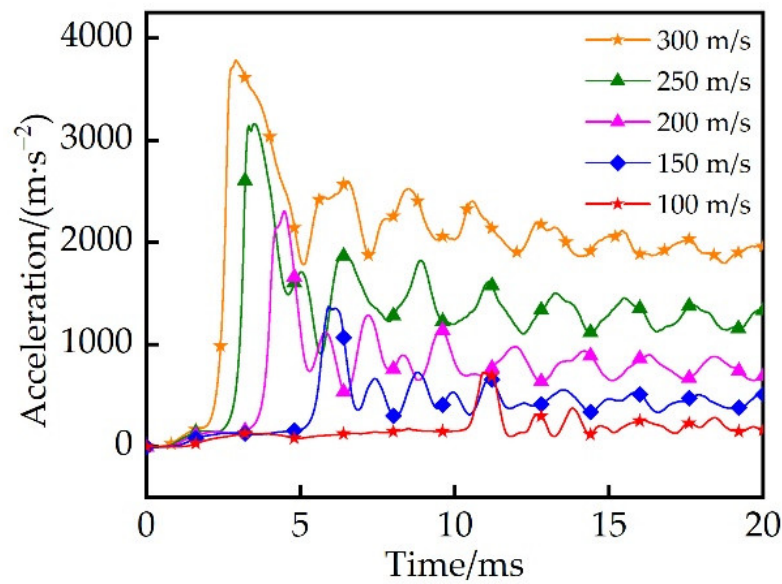


Figure 17. Time-history of acceleration at different speeds of water entry.

4. Characteristic Analysis of Frequency Domain

4.1. Dry Modal Analysis of Vehicle

The structural dynamic response of the vehicle in the process of water entry is an important factor to judge whether the vehicle can enter the water safely. The vibration generated by the vehicle in the process of water entry due to the extreme impact environment is very complex. According to the superposition principle, the complex vibration of the vehicle can be divided into the vibration of several simple and independent subsystems, that is, multi-order modes. In order to further explore the characteristics of the main modes of the vehicle and reveal the actual vibration response of the vehicle under the excitation of external vibration sources in different frequency bands, the dry mode analysis of the fixed end face of the vehicle head is carried out.

Generally, the linear motion equation of the structure can be expressed as:

$$\mathbf{M}\ddot{\mathbf{u}} + \mathbf{C}\dot{\mathbf{u}} + \mathbf{K}\mathbf{u} = \mathbf{F}(t) \tag{8}$$

where \mathbf{M} is the mass matrix, $\ddot{\mathbf{u}}$ is the acceleration vector, \mathbf{C} is the damping matrix, $\dot{\mathbf{u}}$ is the velocity vector, \mathbf{K} is the stiffness matrix, \mathbf{u} is the displacement vector and $\mathbf{F}(t)$ is the external excitation force vector.

For dry mode analysis, the following assumptions are made: (1) the stiffness matrix and mass matrix are unchanged; (2) the system has no damping; (3) the structure has no excitation force; (4) the material characteristic is linear elasticity; (5) small displacement theory is adopted, and non-linear characteristics are not included; (6) the structure may be unconstrained or partially or completely constrained; (7) the modal shape results are relative values, not absolute values.

Since the system damping and excitation force are neglected, the Equation (8) can be simplified as:

$$\mathbf{M}\ddot{\mathbf{u}} + \mathbf{K}\mathbf{u} = \mathbf{0} \tag{9}$$

It is assumed that the vibration of the vehicle shell is a harmonic response motion.

$$\mathbf{u} = \boldsymbol{\varphi}_i \sin(\omega_i t + \theta_i) \tag{10}$$

$$\dot{\mathbf{u}} = \omega_i \boldsymbol{\varphi}_i \cos(\omega_i t + \theta_i) \tag{11}$$

$$\ddot{\mathbf{u}} = -\omega_i^2 \boldsymbol{\varphi}_i \sin(\omega_i t + \theta_i) \tag{12}$$

Equations (10)–(12) are brought into Formula (9) and simplified to obtain:

$$\mathbf{K}\boldsymbol{\varphi}_i - \omega_i^2\mathbf{M}\boldsymbol{\varphi}_i = \mathbf{0} \tag{13}$$

The condition that Equation (13) holds is $\boldsymbol{\varphi}_i = \mathbf{0}$ (no vibration) or $\det(\mathbf{K} - \omega_i^2\mathbf{M}) = 0$. Obviously, the latter is the equation that needs to be solved. This equation is an n -order algebraic equation about ω_i^2 . The n mutually different positive roots obtained by solving this equation are the natural frequencies of the i -order modes. $\boldsymbol{\varphi}_i$ represents the vibration shapes of the structure when it vibrates at the natural frequencies, that is, the mode shapes.

Figure 18 shows the distribution range of the natural frequency. Moreover, Table 10 describes the natural frequencies and corresponding modal modes of the vehicle. From the results of modal analysis, most of the modes of the vehicle appear in pairs, their modal modes are the same, and the corresponding natural frequencies are close. Among them, the 1st mode and the 2nd mode appear in pairs, and the corresponding natural frequency is 4.8392 Hz; the 3rd mode and the 4th mode appear in pairs, and the corresponding natural frequency is 35.527 Hz; the natural frequency corresponding to the 5th mode is 72.868 Hz; the 6th mode and 7th mode appear in pairs, and the corresponding natural frequency is 106.51 Hz; the natural frequency corresponding to the 8th mode is 106.72 Hz; the 9th mode and 10th mode appear in pairs, and the corresponding natural frequency is 109.9 Hz; the 11th order mode and the 12th order mode appear in pairs, and the corresponding natural frequency is 117 Hz; the 13th order mode and the 14th order mode appear in pairs, and the corresponding natural frequency is 139 Hz; the 15th order mode and the 16th order mode appear in pairs, and the corresponding natural frequency is 177 Hz; the 17th order mode and the 18th order mode appear in pairs, and the corresponding natural frequency is 198.38 Hz; the natural frequency corresponding to the 19th mode is 219.54 Hz; the natural frequency corresponding to the 20th mode is 225.34 Hz.

Figure 19 shows the 1st, 8th, 12th and 19th modal modes. From the perspective of the modal modes of the vehicle, the first and second modal modes are swinging, and the rest are composite modal modes of torsion, bending and compression. With the increase in the modal order, the corresponding natural frequency increases, and the orders of bending, wrinkling and vibration increase accordingly.

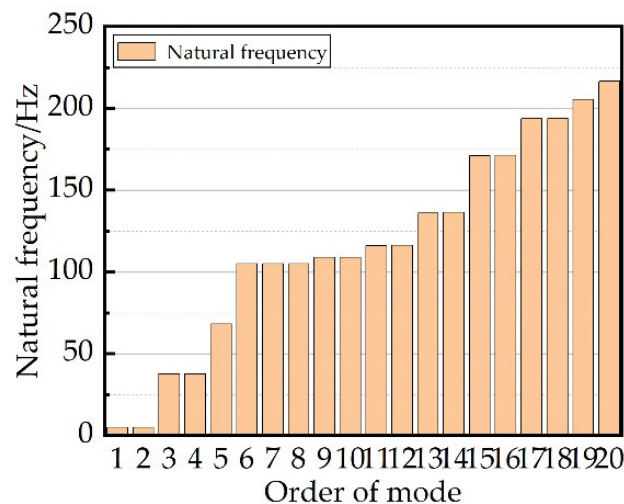


Figure 18. Natural frequency of each order.

Table 10. Natural frequency of vehicle.

Order	Frequency/Hz	Shape	Ratio (x)	Ratio (y)	Ratio (z)
1	5.16	Swing	0.000017	0.806071	1.000000
2	5.16	Swing	0.000019	1.000000	0.806055
3	37.79	First order bending	0.000077	0.539575	0.336182
4	37.79	First order bending	0.000040	0.336190	0.539567
5	68.15	Axial compression	0.000167	0.000004	0.000034
6	105.11	Second order bending	1.000000	0.037302	0.011493
7	105.14	Second order bending	0.116479	0.326490	0.074489
8	105.14	Compression	0.008578	0.075321	0.328600
9	108.95	Axial torsion	0.000003	0.000111	0.000084
10	109.10	Axial torsion	0.000073	0.000046	0.000086
11	116.10	Second order torsion	0.000015	0.000008	0.000020
12	116.31	Second order torsion	0.000045	0.000028	0.000034
13	136.16	Second order torsion	0.000025	0.000003	0.000012
14	136.44	Second order torsion	0.000035	0.000021	0.000031
15	171.10	Third order torsion	0.000011	0.000013	0.000015
16	171.30	Third order torsion	0.000015	0.000008	0.000037
17	193.81	Third order bending	0.000010	0.199081	0.110238
18	193.81	Third order bending	0.000016	0.110245	0.199090
19	205.67	First order compression	0.000035	0.000095	0.000242
20	216.51	Fourth order torsion	0.000024	0.000003	0.000022

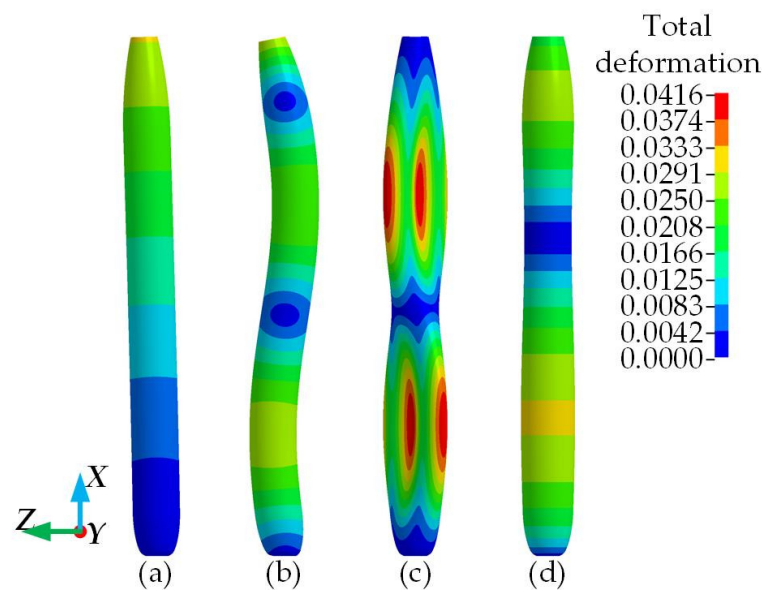


Figure 19. Shapes of 1st, 8th, 12th and 19th mode. (a) 1, (b) 8, (c) 12, (d) 19.

4.2. Shock Response Spectrum Analysis

The impact load of the vehicle entering the water has typical characteristics of impact. The signal of impact load is not a single frequency signal, but a composite signal composed of multiple frequency signals. The spectral decomposition method is widely used in the analysis of impact signal. The shock response spectrum is equivalent in response and the effect on the structure is also equivalent. Therefore, the shock response spectrum simulation can more truly approach the actual impact environment. The improved recursive digital filtering algorithm is used to calculate the shock response spectrum of acceleration [32].

Figure 20 is the shock response spectrum of the acceleration of the vehicle without head cap when it enters the water vertically at the speed of 100 m/s, including the initial response spectrum obtained by taking the corresponding peak value within the impact action time and the residual response spectrum obtained by taking the corresponding peak value after the impact excitation. It can be seen from the figure that the response amplitude

of the shock response spectrum can be roughly divided into three regions. One is the buffer area, where the impact response value of the system is less than the amplitude of the impact pulse. The second is the enlarge area, where the impulse response value of the system is greater than the amplitude of the impulse pulse. The third is the equivalent area, where the impulse response value of the system is approximately equal to the amplitude of the impulse pulse.

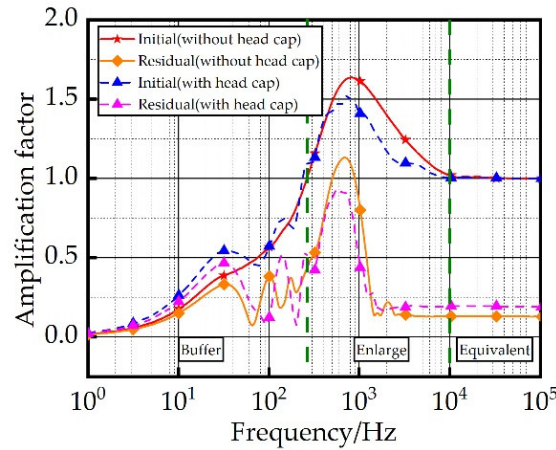


Figure 20. Acceleration shock response spectrum of vehicle vertical water entry at 100 m/s.

The initial response spectrum of the impact load of the vehicle entering the water is taken for analysis. Figure 21 is the initial response spectrum curve of the acceleration at different speed of vehicle without the head cap, and Figure 22 is the initial response spectrum of the acceleration at different speed of vehicle with the head cap. It can be seen from Figure 20 that when the water entry speed is 100 m/s, compared with that without head cap, the initial shock response spectrum of the vehicle entering the water with head cap appears multiple maxima, which indicates that the force situation is more complicated. In addition to the fluid solid coupling force between the vehicle and the water, there is also the force and reaction force between the components of the head cap and the vehicle. When the vehicle does not have the head cap, there is only a maximum value in the initial shock response spectrum. At this time, the force on the vehicle is only the fluid–solid coupling force between the vehicle and the water. When there is no head cap, the pulse width and amplification factor of the enlarged area of the initial shock response spectrum are larger, which can amplify more modal modes of the vehicle. When there is no head cap, the impact excitation has greater damage potential for the shell of the vehicle.

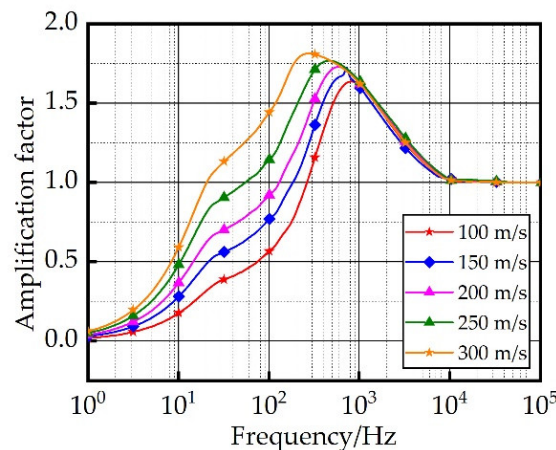


Figure 21. Acceleration shock response spectrum of vehicle without buffer at different speeds of water entry.

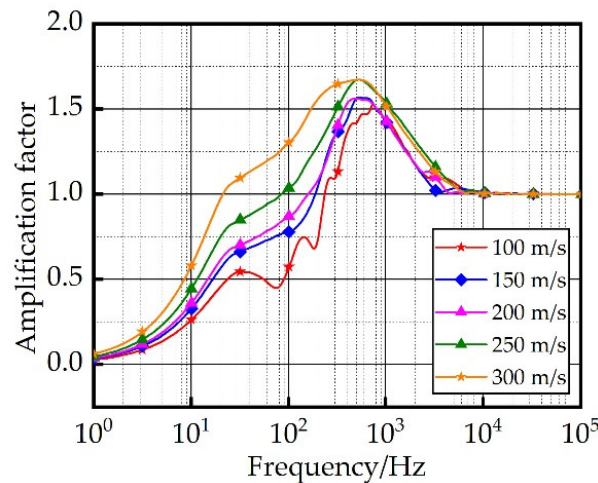


Figure 22. Acceleration shock response spectrum of vehicle with buffer at different speeds of water entry.

Comparing the shock response spectra under different speeds of water entry, it can be seen that with the increase in the water entry speed, the bandwidth of the amplification zone increases, which indicates that the increase in the vehicle’s water entry speed will stimulate more orders and more complex modal modes, and the difference between the two initial impact response spectra will narrow with and without the buffer head cap (Figure 23). This shows that the buffer capacity of the buffer head cap decreases with the increase in the speed of water entry. When the vehicle enters the water at extremely high speed, the buffering effect of the buffer head cap is limited.

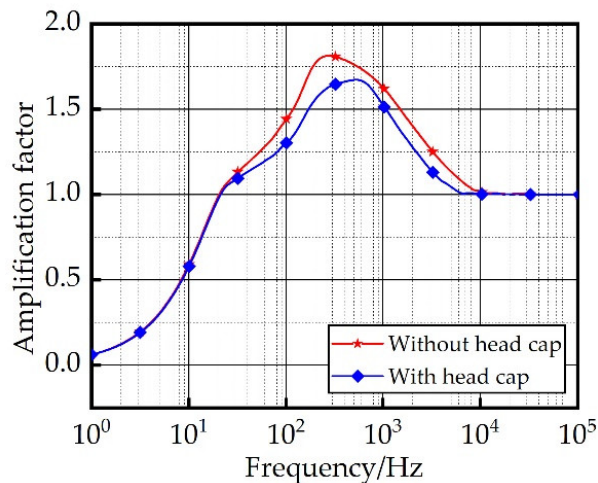


Figure 23. Acceleration shock response spectrum of vehicle vertical water entry at 300 m/s.

4.3. Structural Response Analysis

Since no external load is applied during the modal analysis, the modal deformation obtained from the dry modal analysis of the vehicle is a relative value. In order to understand the actual response of the vehicle shell structure during the process of water entry, the analysis is carried out in combination with the dry modal analysis of the vehicle and the shock response spectrum of acceleration in the commercial software (ANSYS WorkBench).

The response spectrum represents the response of the single degree of freedom system to a time–history load function, and the response can be displacement, velocity, acceleration, force, etc. Considering that the vertical axial force is mainly received during the vertical water entry of the vehicle, the response spectrum analysis is simplified to apply a vertical acceleration response spectrum curve on the end face of the vehicle head along the axial

direction, to determine the response of the vehicle structure to various frequencies of transient excitation or loads.

In the dry mode analysis of the vehicle, the participation factor in the excitation direction is calculated for each mode. The participation factor is a function of the mode shape and the excitation direction, which measures the contribution of the mode to the structural deformation in the excitation direction. The larger the mode shape participation factor of a certain mode in a certain direction, the more the force in the excitation direction will cause a large structural deformation corresponding to this mode. Once the maximum response of each mode under the given response spectrum is obtained, the response is combined according to the correlation coefficient between modes to obtain the total response of the vehicle shell structure. Figure 24 is a schematic diagram obtained by normalizing the modal participation factors. The diagram shows that when the excitation is applied in the X direction, the 6th and 7th modes contribute the most to the structural deformation, and both are bending modes, which indicates that the vehicle structure is mainly subject to bending deformation. When the excitation is applied in Y or Z direction, the multi-order modes contribute to the structural deformation of the vehicle, and the structural deformation is mainly the combination of swing and bending.

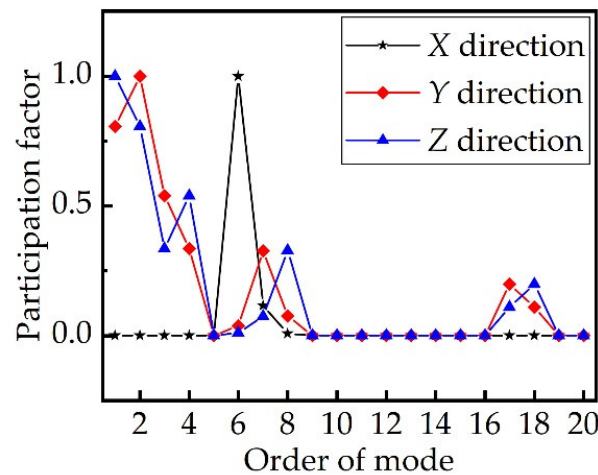


Figure 24. Participation factor of each mode in different direction.

Combined with the acceleration response spectrum of the vehicle, the structural response of the model is solved. Figure 25 shows the structural response of the vehicle when it enters the water vertically at a speed of 100 m/s. It can be seen from the figure that the structural deformation of the vehicle is a combination of compression and bending. Since the end face of the head is fixed, the displacement at the end face of the head is the smallest, the displacement at the tail is the largest, and the deformation from the tail to the head is gradually reduced. As mentioned above, when the excitation is applied in the X direction, the 6th and 7th modes contribute the most to the structural deformation. However, from the results, there is no multi-order deformation similar to the modal mode, which is similar to the buckling of the compression member. Because the length of the vehicle is long, it can be compared to a compression member, and the excitation is applied at the other end of the compression member. When the excitation is small, the deformation of the compression member is mainly compression deformation, and when the excitation is large enough, the compression member will produce instability and multi-order deformation. Comparing Figure 25a with Figure 25b, it can be seen that although the emergence of the head cap cannot avoid the occurrence of compression and bending modes, the head cap significantly reduces the amplitude of the structural response of the vehicle during the water entry process, and has certain beneficial effects on the high-speed and safe water entry of the vehicle.

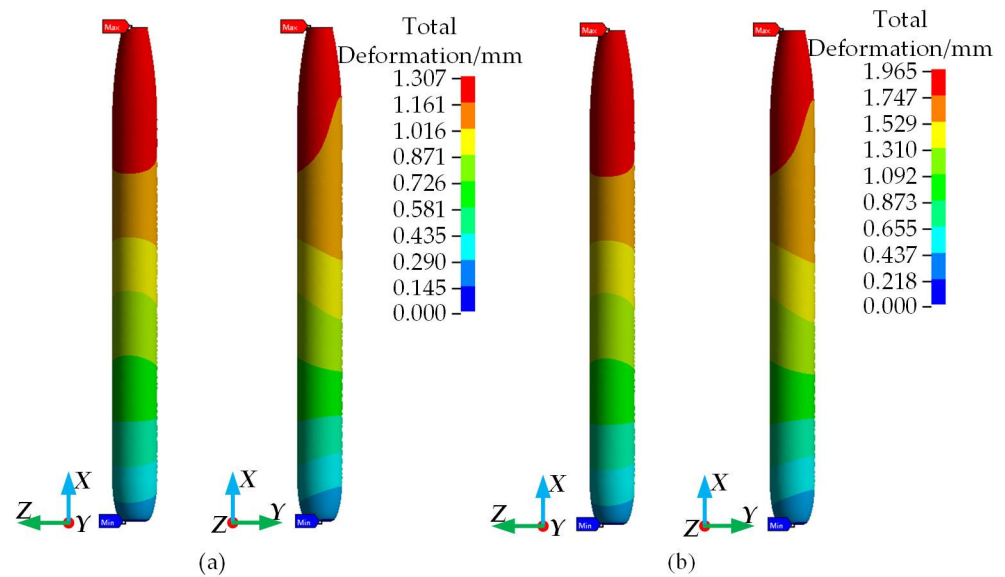


Figure 25. Structural response of the vehicle entering water vertically at speed of 100 m/s, (a) with buffer, (b) without buffer.

5. Conclusions

An ALE-based numerical model of LS-DYNA was employed to study the high-speed water entry of a vehicle, analyze the changes of load and cavity of flow field during the water entry of the vehicle, and combine modal analysis and shock response spectrum to analyze dynamic characteristics such as the structural response of the vehicle shell during water entry. The main conclusions were as follows:

- (1) Affected by the head cap at the early stage of water entry, the cavity is larger and its wall is rougher. At the later stage of water entry, the head cap is separated from the vehicle, and the wall of cavity gradually separates from the influence of the head cap and is basically the same when there is no head cap.
- (2) The peak value and pulse width of the impact load increase with the increase in the speed of water entry, and the load reduction effect of the head cap decreases with the increase in the speed of water entry. The change trend of the time–history of impact load is greatly affected by the compression mechanical characteristics of the buffer material itself.
- (3) The structural response of the vehicle in the process of water entry is mainly composed of compression deformation and bending deformation. The head cap can reduce the amplitude of the structural response. When the impact load is small, the vehicle will mainly undergo compression deformation. When the impact load is large enough, a phenomenon similar to the buckling of compression member will appear.

Author Contributions: Conceptualization and methodology, all authors; design of simulation ideas, Z.L. and H.Z.; setting of simulation cases, sorting and analysis of data, visualization of results and writing—original draft, Z.L.; writing—review and editing, Y.S. and Z.L.; management of project, supporting of funding and equipment, Y.S. and G.P. All authors have read and agreed to the published version of the manuscript.

Funding: The research was supported by the National Natural Science Foundation of China (Grant No. U21B2055, Grant No. 52171324) and the Fundamental Research Funds for the Central Universities (Grant No. 3102019JC006).

Institutional Review Board Statement: Not applicable.

Informed Consent Statement: Not applicable.

Data Availability Statement: All data and models generated or used during the research period appear in the submitted manuscript.

Conflicts of Interest: The authors have no conflict of interest and unanimously agree to submit the manuscript to the journal.

References

1. Wang, H.Y.; Li, M.Y.; Cheng, S.H.; Zhang, X.C. Review of vehicle's high-speed water entry. *Astronaut. Syst. Eng. Technol.* **2021**, *5*, 65–70. (In Chinese)
2. Miloh, T. On the oblique water-entry problem of a rigid sphere. *J. Eng. Math.* **1991**, *25*, 77–92. [[CrossRef](#)]
3. Reinhard, M.; Korobkin, A.A.; Cooker, M.J. Water entry of a flat elastic plate at high horizontal speed. *J. Fluid Mech.* **2013**, *724*, 123–153. [[CrossRef](#)]
4. Hulin, F.; Del Buono, A.; Tassin, A.; Bernardini, G.; Iafrati, A. Gravity effects in two-dimensional and axisymmetric water impact models. *J. Fluid Mech.* **2022**, *944*, A9. [[CrossRef](#)]
5. Ryzhakov, P.; Rossi, R.; Viña, A.; Oñate, E. Modelling and simulation of the sea-landing of aerial vehicles using the Particle Finite Element Method. *Ocean Eng.* **2013**, *66*, 92–100. [[CrossRef](#)]
6. Sun, Y.S.; Zhou, S.H.; Zhang, X.B.; Xiang, Y.L. On water-impact load of heavy projectiles base on multi-material ALE method. *J. Nav. Univ. Eng.* **2019**, *31*, 101–106. (In Chinese)
7. Wang, M.Z.; Cao, D.F.; Wu, B.; Hu, H.X.; An, Z.J.; Yuan, Z.D. Numerical analysis of aircraft dynamic behavior in ditching based on S-ALE fluid-structure interaction method. *J. Chongqing Univ.* **2020**, *43*, 21–29. (In Chinese)
8. He, G.H.; Xie, B.Y.; Wang, W.; Liu, S.; Jing, P.L. Ship Loading Influence on the Slamming Impact of Typical Sections of an S-175 Container Ship. *J. Mar. Sci. Eng.* **2020**, *8*, 163. [[CrossRef](#)]
9. Li, Y.; Sun, T.Z.; Zong, Z.; Li, H.T.; Zhao, Y.G. Dynamic crushing of a dedicated buffer during the high-speed vertical water entry process. *Ocean Eng.* **2021**, *236*, 109526. [[CrossRef](#)]
10. Wei, H.P.; Shi, C.B.; Sun, T.Z.; Bao, W.C.; Zhang, G.Y. Numerical study on load-shedding performance of a high-speed water-entry vehicle based on an ALE method. *Explos. Shock Waves* **2021**, *41*, 104201-1–104201-12. (In Chinese)
11. Sun, L.Q.; Wang, D.L.; Li, Z.P.; Liu, D.K. Analysis on load reduction performance of foamed aluminum buffer device for high speed water entry of vehicle based on a CEL method. *J. Vib. Shock.* **2021**, *40*, 80–88. (In Chinese)
12. Quan, X.B.; Bao, J.; Sun, L.Q.; Wang, D.L. Impact performance of cushion nose cap of underwater vehicle based on CEL method. *Acta Armamentarii* **2022**, *43*, 851–860. (In Chinese)
13. Yu, P.Y.; Shen, C.; Zhen, C.B.; Tang, H.Y.; Wang, T.L. Parametric study on the free-fall water entry of a sphere by using the rans method. *J. Mar. Sci. Eng.* **2019**, *7*, 122. [[CrossRef](#)]
14. Qiu, S.Y.; Ren, H.X.; Li, H.J. Computational model for simulation of lifeboat free-fall during its launching from ship in rough seas. *J. Mar. Sci. Eng.* **2020**, *8*, 631. [[CrossRef](#)]
15. Li, Q.; Lu, L. Numerical investigations of cavitation nose structure of a high-speed projectile impact on water-entry characteristics. *J. Mar. Sci. Eng.* **2020**, *8*, 265. [[CrossRef](#)]
16. Yang, Q.Z.; Xu, F.; Yang, Y.; Wang, J.Y.; Wang, A.W.; Ma, C.H. Numerical study on the dynamic characteristics of water entry of cavity body using two-phase SPH method. *Acta Mech. Sin.* **2021**, *37*, 1072–1089. [[CrossRef](#)]
17. Sun, Z.; Sui, X.P.; Deng, Y.Z.; Zuo, L.; Korobkin, A.; Xu, L.X.; Jiang, Y.C. Characteristics of slamming pressure and force for trimaran hull. *J. Mar. Sci. Eng.* **2021**, *9*, 564. [[CrossRef](#)]
18. Fan, C.Y.; Wang, M.; Li, H. High speed water entry phenomenon comparison of projectile with free and constant speed. *J. Appl. Phys.* **2022**, *132*, 064701. [[CrossRef](#)]
19. Wang, H.; Luo, Y.C.; Chen, Z.H.; Guo, Z.Q.; Huang, Z.G. Influences of ice-water mixture on the vertical water-entry of a cylinder at a low velocity. *Ocean Eng.* **2022**, *256*, 111464. [[CrossRef](#)]
20. Chen, C.; Ma, Q.; Wei, Y.; Wang, C. Experimental study on the cavity dynamics in high-speed oblique water-entry. *Fluid Dyn. Res.* **2018**, *50*, 045511. [[CrossRef](#)]
21. Panciroli, R.; Pagliaroli, T.; Minak, G. On air-cavity formation during water entry of flexible wedges. *J. Mar. Sci. Eng.* **2018**, *6*, 155. [[CrossRef](#)]
22. Zhou, J.; Xu, S.L.; Peng, J. Water entry flow-field visualization of oblique penetration of a high-speed projectile. *Chin. J. High Press. Phys.* **2018**, *32*, 132–139. (In Chinese)
23. Chen, T.; Huang, W.; Zhang, W.; Qi, Y.F.; Guo, Z.T. Experimental investigation on trajectory stability of high-speed water entry projectiles. *Ocean Eng.* **2019**, *175*, 16–24. [[CrossRef](#)]
24. Song, Z.J.; Duan, W.Y.; Xu, G.D.; Zhao, B.B. Experimental and numerical study of the water entry of projectiles at high oblique entry speed. *Ocean Eng.* **2020**, *211*, 107574. [[CrossRef](#)]
25. She, W.X.; Guo, C.Y.; Zhou, G.L.; Wu, T.C.; Xu, P. Time-Resolved PIV measurements and numerical study of water entry of a wedge. *J. Shanghai JiaoTong Univ.* **2020**, *54*, 839–848. (In Chinese)
26. Liu, E.W.; Xu, S.L.; Zhou, J.; Zuo, J.D. Development of gas guns combined with a water tank for launching high-velocity projectiles into water obliquely and horizontally. *Explos. Shock Waves* **2022**, *42*, 99–109. (In Chinese)

27. Sun, T.Z.; Wang, S.S.; Bai, P.Y.; Ren, W.C. Cavity dynamics of water entry for a head-ventilated cylinder. *Phys. Fluids* **2022**, *34*, 073302. [[CrossRef](#)]
28. Tang, S.Q.; Zhang, Y.; Sun, S.L.; Ren, H.L.; Zhang, H.B.; He, J.H. Experimental investigation on the air-cushion effect during free fall of a trimaran section using an air escape control method. *Ocean Eng.* **2022**, *254*, 111417. [[CrossRef](#)]
29. Shi, Y.; Liu, Z.P.; Pan, G.; Gao, X.F. Structural design and load reduction performance analysis of gradient density head cap of vehicle. *Chin. J. Mech.* **2022**, *54*, 939–953. (In Chinese)
30. Qian, L.X.; Liu, F.; Qu, M.; Hu, Y.H.; Zhao, J.B. Failure mode of torpedo nose cap in water-entry. *Torpedo Technol.* **2015**, *23*, 257–261. (In Chinese)
31. Hirt, C.W.; Amsden, A.A.; Cook, J.L. An arbitrary Lagrangian–Eulerian computing method for all flow speeds. *J. Comput. Phys.* **1997**, *135*, 203–216. [[CrossRef](#)]
32. Smallwood, D.O. An improved recursive formula for calculating shock response spectra. *Shock. Vib.* **1981**, *51*, 211–217.